Nano Research

Open Access

Research Article

Unraveling the activation insight of molecular oxygen in oxygen vacancy-enriched Cu/Cu_2O Schottky junctions with dual LSPR effect toward high-efficient NIR light-driven photothermal catalysis

Haotian Wang[1], Shaodong Sun[1,2] ✉, Wenshao Lin[1], Hua Chang[1], Xiaojing Yu[1], Qing Yang[1], Man Yang[1,2] ✉, and Jie Cui[1,2] ✉

[1] *Engineering Research Center of Conducting Materials and Composite Technology, Ministry of Education; Shaanxi Engineering Research Center of Metal-Based Heterogeneous Materials and Advanced Manufacturing Technology; Shaanxi Province Key Laboratory for Electrical Materials and Infiltration Technology; School of Materials Science and Engineering, Xi'an University of Technology, Xi'an 710048, China*
[2] *Shaanxi Laboratory of Advanced Materials, Xi'an 710018, China*

Cite this article: *Nano Research*, **2026**, *19*, 94908781. https://doi.org/10.26599/NR.2026.94908781

ABSTRACT: The development of efficient near-infrared (NIR) light-driven Cu_2O-based photocatalysts and a deeper understanding of their underlying mechanisms for pollutant degradation are urgently needed. Herein, we report the rational design of oxygen vacancy-enriched Cu/Cu_2O Schottky junctions via H_2MoO_4-template-assisted liquid-phase reduction method. Under NIR irradiation, the optimized Cu/Cu_2O composite exhibits remarkable photothermal catalytic performance, achieving 85.1% degradation of tetracycline within 120 min. The enhanced activity is attributed to the synergistic effect of the Schottky junction, dual localized surface plasmon resonance (LSPR), and a unique "directional anchoring" mechanism for O_2 activation. First, the Schottky junction formed at the Cu/Cu_2O interface promotes efficient separation of photogenerated charges. Second, a dual LSPR effect, combining the intrinsic LSPR of Cu nanoparticles with the defect-state LSPR induced by oxygen vacancies, significantly enhances NIR light absorption and photothermal conversion efficiency. Most importantly, *in-situ* spectroscopic and density functional theory analyses reveal a unique "directional anchoring" mechanism for O_2 activation at the oxygen vacancy (OV)-Cu interface. In this process, O_2 is selectively captured at the OV–Cu dual sites, where electron transfer from the interface weakens the O–O bond, thereby facilitating the generation of reactive oxygen species. This work provides fundamental insights into the design of high-performance NIR-driven photothermal catalysts for environmental remediation.

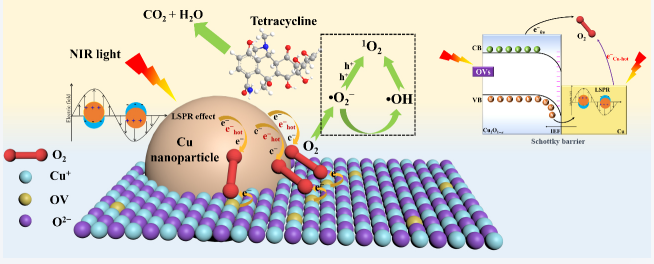

KEYWORDS: Cu_2O, Schottky junction, oxygen vacancy, near-infrared (NIR) light, localized surface plasmon resonance (LSPR) effect, oxygen activation

1 Introduction

The escalating global crisis of aquatic pollution, primarily driven by the excessive discharge of antibiotics from healthcare and agricultural activities, underscores the urgent need for advanced water remediation technologies [1–6]. Among various strategies, photocatalytic oxidation has attracted significant interest due to its ability to harness solar energy for generating reactive oxygen species (ROS), which can mineralize refractory organic pollutants into harmless substances [7–12]. However, a major limitation of conventional wide-bandgap semiconductors is their poor utilization of near-infrared (NIR) light, which accounts for nearly half of the solar spectrum [13–16]. This mismatch highlights the critical importance of developing novel photocatalytic systems capable of efficient NIR photon conversion.

Recently, research has increasingly focused on localized surface plasmon resonance (LSPR), a phenomenon in which collective oscillations of free electrons in metal nanostructures under light illumination enhance local electromagnetic fields [16–18]. The integration of LSPR-active nanomaterials with semiconductors has shown promise in broadening the light absorption range and

Received: March 16, 2026; **Revised:** April 23, 2026
Accepted: April 27, 2026

✉Address correspondence to Shaodong Sun, sdsun@xaut.edu.cn; Man Yang, myang@xaut.edu.cn; Jie Cui, cuijie@xaut.edu.cn

improving charge separation, thereby overcoming some limitations of traditional ultraviolet (UV) and visible-light-driven photocatalysis [19–22]. Nevertheless, this approach faces two major bottlenecks. Firstly, the field heavily relies on noble metals like gold and silver, whose cost and scarcity hinder practical application. While non-noble Cu is an attractive alternative due to its Earth-abundance and strong NIR LSPR, its integration into efficient and stable photocatalytic architectures remains less explored. Secondly, and more importantly, the mechanistic understanding of LSPR-mediated enhancement remains superficial. The contribution is frequently attributed to photothermal effects and extended light absorption, while the specific role of LSPR-generated hot electrons in critical redox processes, particularly the activation pathway of molecular oxygen, is not fully elucidated. Parallel to developments in plasmonic, defect engineering, particularly the introduction of oxygen vacancies (OVs), has emerged as a powerful strategy for tuning the electronic structure of metal oxides [23, 24]. At high concentrations, OVs can generate enough free carriers to induce a defect-state LSPR effect, endowing the semiconductor itself with metal-like optical properties [25, 26]. This phenomenon is particularly well-established in non-stoichiometric oxides such as WO_{3-x}, MoO_{3-x}, and $W_{18}O_{49}$ [27–29], where high carrier densities trigger collective oscillations in the NIR region. Cu_2O has been regarded as a classic p-type semiconductor with visible light absorption (~ 2.1 eV), recent breakthroughs on Cu_2O_{1-x} superlattices have successfully demonstrated that vacancy engineering can induce a robust defect-state LSPR effect, significantly extending the optical response of Cu_2O into the NIR range [26]. In particular, the localized photothermal effect has been identified in recent studies as a crucial driver for accelerating surface reaction kinetics and effectively lowering the activation energy barriers in catalytic systems [30, 31]. Furthermore, the positively charged environment around OVs facilitates electron transfer to adsorbed O_2, promoting its reduction to various ROS [32–35]. However, the synergistic combination of metallic LSPR (from Cu) and defect-state LSPR (from OVs) within a single composite material, along with its precise effect on the molecular oxygen activation mechanism, remains a significant research gap, necessitating integrated experimental and theoretical investigation.

Herein, we successfully synthesized oxygen vacancy-enriched Cu/Cu_2O using a H_2MoO_4-template-assisted method. The *in-situ* formation of Cu within Cu_2O establishes a Schottky junction that promotes efficient charge separation. Moreover, the composite exhibits a dual LSPR effect, arising from the intrinsic LSPR of Cu and the defect-state LSPR induced by OVs, which together enhance NIR light harvesting and produce a strong photothermal response. Most importantly, this study offers deep insight into the O_2 activation process through a combination of *in-situ* characterization and density functional theory (DFT) calculations. Results uncover a "directional anchoring" mechanism at the OV-Cu interface, where one oxygen atom fills a vacancy site on Cu_2O while the other interacts with an adjacent Cu atom. This configuration, coupled with efficient electron transfer via the interfacial Schottky interface, significantly weakens the O–O bond. Thus, this work not only demonstrates an efficient NIR-driven photothermal catalyst but also offers fundamental insights into the synergistic roles of interface engineering and dual LSPR effects, advancing the design principles for non-noble metal-based photocatalytic materials.

2 Experimental section

Synthesis of catalysts: The Cu/Cu_2O composites were synthesized by a H_2MoO_4 template-assisted liquid-phase reduction method. As part of the standard protocol for the synthesis of Cu/Cu_2O composites, 75 mg of H_2MoO_4 powder and $Cu(NO_3)_2{\cdot}3H_2O$ (0.6 M, 1 mL) were added into a round-bottomed flask that held 25 mL of EG solution before being dispersed via sonication for a 10-minute period. The flask was moved to an oil bath set at 90 °C and heated for 10 min, and a mixture of EG (5 mL) and NaOH solution (3 M, 1 mL) was dropped into the mixed solution. Subsequently, 0.4 g of D-isoascorbic acid Na ($C_6H_7O_6Na$) was added to the aforementioned solution, then held for 40 min. Finally, the prepared Cu/Cu_2O composites were washed by ethanol centrifugation (10,000 r·min^{-1}, 4 min) and dried at 60 °C. For comparative purposes, the Cu_2O sample was similarly prepared under identical conditions in the absence of H_2MoO_4.

Analytical methods and catalytic activity evaluation: Microstructural characterizations, physicochemical measurements, and photocatalytic performance tests and method of DFT calculations were provided in the Electronic Supplementary Material (ESM).

3 Results and discussion

3.1 Morphology and structural characterization

Figures 1(a) and 1(b) depict the schematic diagrams of the synthesis of Cu_2O and Cu/Cu_2O products by the H_2MoO_4-assisted liquid-phase reduction method. Before introducing the reductant, $Cu(NO_3)_2$ dissociates in EG solvent, yielding Cu^{2+} ions. Upon adding NaOH, the increased alkalinity promoted the combination of Cu^{2+} with OH^- to form $Cu(OH)_2$. Finally, Cu_2O and Cu/Cu_2O were produced after adding reducer ($C_6H_7O_6Na$). The possible growth mechanism is discussed in the ESM. As shown in Fig. 1(a), the introduction of $C_6H_7O_6Na$ into the $Cu(NO_3)_2$/NaOH/EG mixture without H_2MoO_4 results in the formation of light yellow Cu_2O precipitates with limited OVs. The formation of OVs is determined by the solvent of EG, which might be similar to that occurring in previous Refs. [36, 37]. In contrast, when H_2MoO_4 was present (Fig. 1(b)), the formed Cu_2O is further reduced by $C_6H_7O_6Na$ in EG solvent to yield metallic Cu, ultimately transforming into Cu/Cu_2O composite as the reaction proceeds. Figure 1(c) shows the transmission electron microscope (TEM) image of Cu_2O samples synthesized without H_2MoO_4 (the inset is the corresponding high-magnification TEM, revealing monodisperse nanospheres with an average size of 80 nm). The lattice spacings marked by the white lines and arrows in Fig. 1(d) are assigned to the (200) planes of Cu_2O. Figure 1(e) displays the TEM image of samples prepared with adding H_2MoO_4 templates (the inset is high-magnification TEM), where the original Cu_2O monodisperse nanospheres transform into a core–shell architecture featuring a Cu core surrounded by dispersed Cu_2O nanospheres as the shell. The high-resolution TEM (HRTEM) image in Fig. 1(f) reveals two distinct lattice spacings marked with white lines and arrows, corresponding to the (200) planes of Cu crystals and (200) planes of Cu_2O.

The crystal phases of the as-synthesized Cu_2O and Cu/Cu_2O composites were characterized using X-ray diffraction (XRD). According to the Fig. 2(a), the diffraction peaks of the sample synthesized in the absence of H_2MoO_4 (black pattern) are

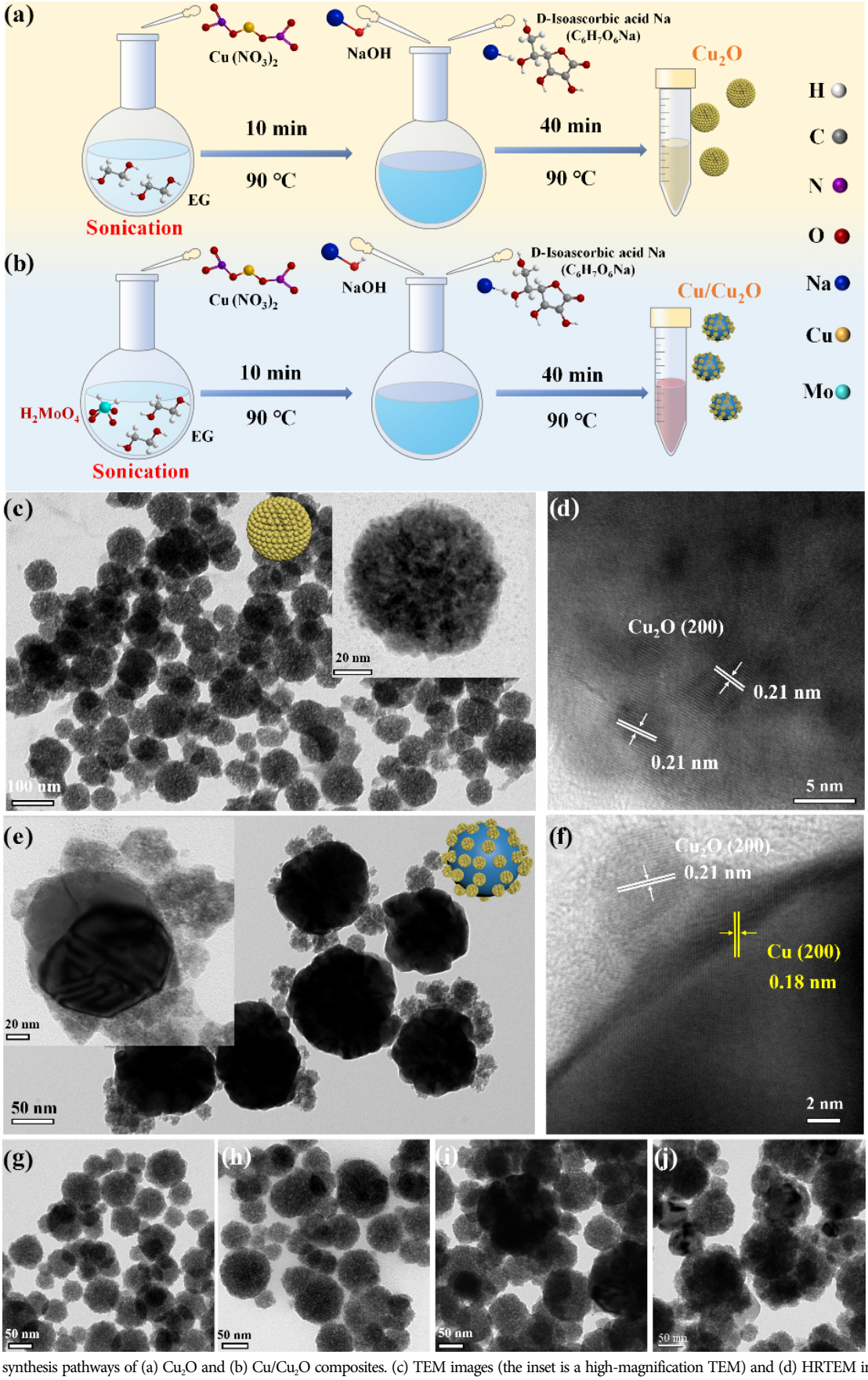

Figure 1 The synthesis pathways of (a) Cu_2O and (b) Cu/Cu_2O composites. (c) TEM images (the inset is a high-magnification TEM) and (d) HRTEM image of Cu_2O. (e) TEM images (the inset is a high-magnification TEM) and (f) HRTEM image of Cu/Cu_2O composites. (g)–(j) TEM images and corresponding schematic diagrams of the different products obtained at 5, 10, 20, 30 min, respectively.

exclusively indexed to pure cubic Cu_2O crystal (matching the JCPDS No. 05-0667), with no evidence of extraneous phases. The product obtained after adding H_2MoO_4 is consistent with the cubic Cu_2O crystal (JCPDS No. 05-0667) and the Cu crystal (JCPDS No. 04-0836). No diffraction peaks related to H_2MoO_4 are detected (see the red pattern). Notably, the diffraction peak clearly observed at 42.3° corresponds to the (200) facets of the Cu_2O crystal, and the diffraction peak at 50.4° corresponds to the (200) facets of the Cu crystal, respectively.

To identify the elemental species and valence states of Cu and O, the as-prepared samples were analyzed by X-ray photoelectron spectroscopy (XPS) and electron paramagnetic resonance (EPR). For the Cu/Cu_2O sample, the survey XPS spectra (Fig. S1(a) in the ESM) show that only copper and oxygen elements are presented, while the molybdenum element is not detected. The absence of characteristic Mo peaks in the survey spectrum confirms the complete consumption of H_2MoO_4 sacrificial templates during the synthesis process. In the high-resolution results of Cu 2p (Fig. 2(b)), the characteristic peaks at 932.1 and 951.8 eV correspond to Cu $2p_{3/2}$ and Cu $2p_{1/2}$ of Cu(0). The core-level peak-peak difference between Cu $2p_{1/2}$ and Cu $2p_{3/2}$ regions is 19.7 eV, which confirms the presence of Cu(0) [38]. The characteristic peaks at 932.7 and 952.6 eV correspond to Cu $2p_{3/2}$ and Cu $2p_{1/2}$ of Cu(I), the characteristic peak at 941.0 eV is the satellite peak. Furthermore, the characteristic peaks located at 934.3 and 954.1 eV, as well as the satellite peaks located at 943.6 and 962.6 eV correspond to the Cu $2p_{3/2}$ and Cu $2p_{1/2}$ of Cu(II) species, respectively, which may be due to the surface oxidation of Cu(I) [39]. The high-resolution spectrum of O 1s (Fig. 2(c)) displays peaks at 530.3, 531.3, and 531.9 eV for the Cu_2O sample. These binding energies correspond to lattice oxygen ($O_{lattice}$), OVs, and surface-adsorbed oxygen ($O_{adsorbed}$) species from the air, respectively. The high-resolution results of O 1s of the Cu/Cu_2O sample reveal three characteristic oxygen species peaks at 530.5, 531.6, and 532.4 eV (Fig. 2(d)), corresponding to $O_{lattice}$, OVs, and $O_{adsorbed}$ species, respectively. This confirms the formation of oxygen vacancies within the Cu/Cu_2O composites [40, 41]. Notably, the Cu_2O samples reduced by a weak reducing agent in EG solvent all contain a certain amount of OVs, which can be attributed to the reduction of EG. Moreover, due to the introduction of H_2MoO_4, the formation energy of OVs was reduced through charge compensation of MoO_4^{2-}. During continuous reduction, $O_{lattice}$ in Cu_2O were further removed, significantly increasing the density of OVs. Consequently, the content of OVs in the Cu/Cu_2O sample is higher than that in the Cu_2O sample (Fig. 2(e)). The corresponding EPR results show that the OVs signal of the Cu/Cu_2O sample is significantly stronger than the Cu_2O sample (Fig. 2(f)), which also indicates that a relatively larger number of OVs are formed on the surface of Cu/Cu_2O sample.

To elucidate the formation mechanism of Cu_2O and Cu crystals in the Cu/Cu_2O composites, TEM images and morphological schematic diagrams of different products were captured at 5, 10, 20, and 30 min. As shown in Fig. 1(g), the initial product consists of spherical aggregates composed of numerous Cu_2O nanospheres. As the reaction time was 10 min (Fig. 1(h)), continued deposition of Cu_2O nanospheres on the aggregate surfaces leads to size enlargement. As the reaction time was 20 min (Fig. 1(i)), morphological transformation occurs as Cu_2O within the aggregates is further reduced to Cu crystal. As the reaction time prolonged to 30 min (Fig. 1(j)), EG and $C_6H_7O_6Na$ further reduce Cu_2O, driving outward growth of internal Cu crystals and gradual formation of the core–shell structure. Ultimately, continued Cu expansion reduces the Cu_2O shell thickness, exposing Cu surfaces and finalizing the evolution into a core–shell structure with Cu_2O nanospheres dispersed on Cu crystals. The XRD patterns of the products obtained at different reaction times confirm the generation of Cu crystal (Fig. S2(b) in the ESM). Characteristic peaks belonging to Cu crystals can be clearly observed in the XRD

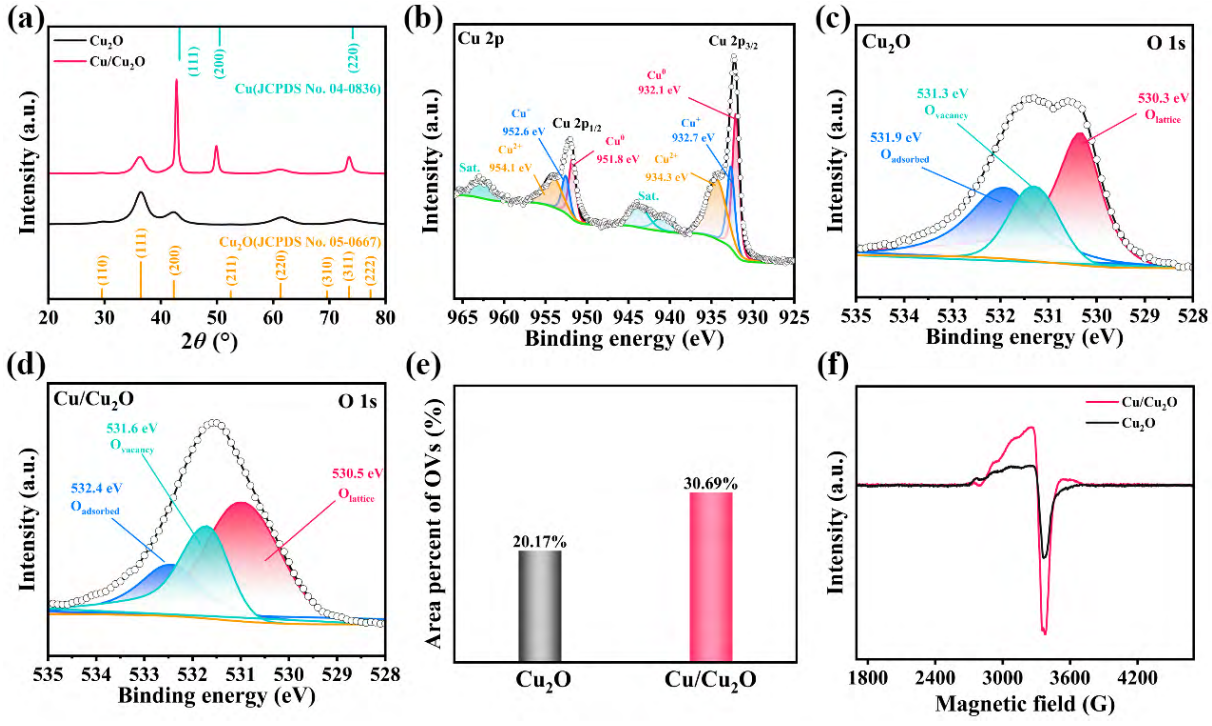

Figure 2 (a) XRD patterns of Cu_2O and Cu/Cu_2O samples. (b) High-resolution XPS results of the Cu 2p for Cu/Cu_2O. High-resolution O 1s spectrum: (c) Cu_2O and (d) Cu/Cu_2O samples. (e) The concentration of OVs of Cu/Cu_2O and Cu_2O samples. (f) EPR spectra of Cu_2O and Cu/Cu_2O powders.

pattern after 20 min. Notably, the prepare principle and pathway of the Cu/Cu_2O composites with rich-OVs are described in the ESM.

3.2 Photophysical properties

UV–vis–NIR diffuse reflectance spectroscopy (UV–vis–NIR DRS) was employed to evaluate the light absorption properties of the catalysts. As shown in Fig. 3(a), Cu/Cu_2O displayed typical light absorption in both the visible and NIR regions, whereas Cu_2O showed a clear visible light response. The fabricated Cu/Cu_2O composites exhibit a broader NIR absorption range than the pure Cu_2O sample, suggesting an enhanced NIR response in the Cu/Cu_2O composites. It is ascribed to the LSPR effect of Cu in the core–shell structure under NIR light range. The Cu/Cu_2O composites can hold a great potential in forming strong plasmon energy and extending the plasmon excitation range to the NIR region. The release of strong plasmon energy in the form of heat will significantly enhance the photothermal performance of the Cu/Cu_2O composites. The Kubelka–Munk method yields a bandgap energy (E_g) of 1.91 eV for Cu_2O (Fig. 3(b)). In contrast, the absence of a band gap in Cu/Cu_2O sample is due to the presence of OVs and Cu, which caused the catalyst as metalloid characteristics.

To confirm the photothermal effect driven by improved NIR absorption, we measured the temperature profiles of Cu/Cu_2O and Cu_2O powders (Fig. S3 in the ESM) using an online thermal camera. As shown in Fig. 3(c), under NIR light irradiation, the temperature of the Cu/Cu_2O sample increased significantly, reaching approximately 99.4 °C in 400 s. In contrast, under the same conditions, the temperature of the Cu_2O sample only reached 77.4 °C. As the irradiation time extended, the temperatures of Cu_2O and Cu/Cu_2O powders could stabilize at 82.9 and 103.9 °C (Fig. 3(d)), respectively. This indicates that the enhancement of the photothermal effect is proportional to the NIR light absorption. Cyclic photothermal stability tests of Cu/Cu_2O were carried out using NIR light (Fig. 3(e)). The results demonstrate that after five "on-off" cycles, Cu/Cu_2O still maintained remarkable photothermal efficiency, thus confirming its photothermal stability. To quantitatively assess the NIR-to-thermal conversion capability, the photothermal conversion efficiency (η) was calculated. The η value for Cu/Cu_2O reached 45.1% in solution conditions (see Section 4.2 in the ESM) [42, 43]. This result further demonstrates the efficiency of the prepared Cu/Cu_2O dual LSPR effect in capturing and converting NIR photons.

Subsequently, the electric field enhancement characteristics of different samples were simulated using the finite-difference time-domain (FDTD) method. The particle model was established through refined optimization based on TEM images (Fig. S5 in the

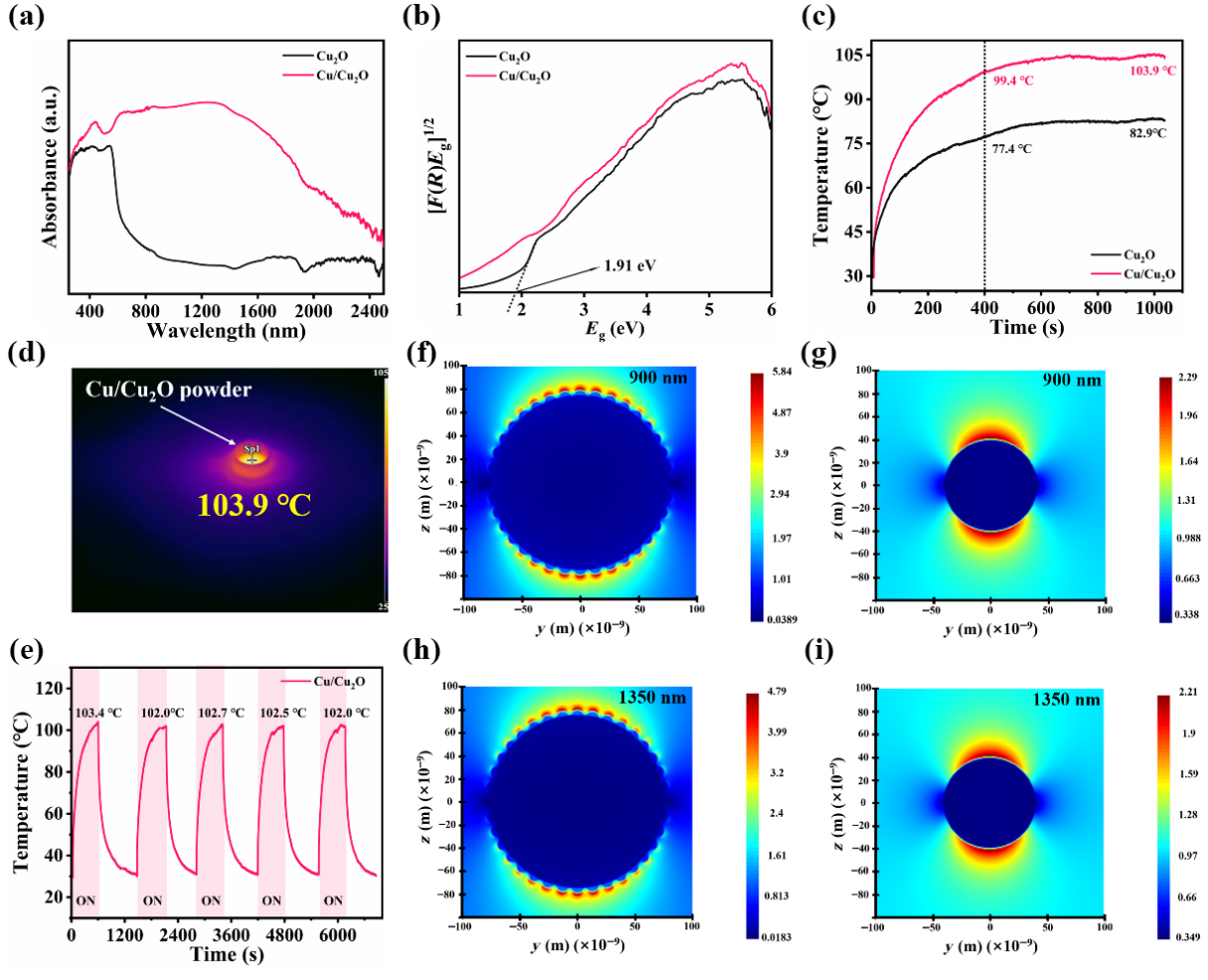

Figure 3 (a) UV–vis–NIR DRS spectra and (b) the corresponding Kubelka–Munk transformed reflectance spectra of the Cu_2O and Cu/Cu_2O samples. (c) The photothermal curves of the Cu_2O and Cu/Cu_2O powder. (d) Infrared thermography images of the Cu/Cu_2O powder after NIR light irradiation. (e) Cyclic thermogenesis of the Cu/Cu_2O composites over 5 "On-Off" detection. The FDTD simulated electric-field spatial distribution on *x*-*y* plane of Cu/Cu_2O and Cu_2O samples under ((f) and (g)) 900 nm and ((h) and (i)) 1350 nm light irradiation.

ESM). As shown in Fig. 3(f), under illumination at the NIR light (900 nm), the Cu/Cu_2O sample comprising Cu nanoparticles decorated with Cu_2O particles exhibited the most pronounced electric field enhancement, amplifying the incident electric field by a factor of 5.84. In contrast, pure Cu_2O particles achieved an enhancement of only 2.29-fold (Fig. 3(g)). Additionally, an electric field increase of approximately 2–3-fold was observed at the Cu-Cu_2O interface (Fig. 3(f)), suggesting that the LSPR properties of Cu can optimize the electric field enhancement on the catalyst surface under NIR light, thereby improving its photocatalytic performance. Furthermore, within a higher wavelength range (1350 nm), the catalyst maintained consistent electric field enhancement trends (Figs. 3(h) and 3(i)). Notably, Cu nanoparticles decorated with Cu_2O particles sustained an enhancement factor of 4.79 (Fig. 3(h)), indicating robust NIR electric field enhancement capabilities.

To further reveal the intrinsic electronic structure mechanism underlying the improved charge separation and transport properties, the work functions (Φ) of Cu_2O and Cu were determined from the electrostatic potential of the Cu_2O(100) plane and Cu(100) plane. Calculation of the energy difference between the Fermi level (E_f) and the vacuum level yields work functions of 6.92 eV (Fig. S6(a) in the ESM) for Cu_2O and 4.34 eV for Cu (Fig. S6(b) in the ESM). When a heterojunction interface was formed between Cu_2O and Cu, due to the significant difference in their work functions, a remarkable band bending phenomenon occurred at the contact interface. According to the band alignment theory, electrons will migrate directionally from Cu with a lower work function (4.34 eV) to Cu_2O with a higher work function (6.92 eV) until the system reaches a thermodynamic equilibrium state and the Fermi level (E_F) becomes consistent. Finally, a Schottky barrier was formed at the interface, which can effectively promote the separation of photocharge (Fig. 4(a)).

The carrier dynamics were elucidated by steady-state photoluminescence (PL) and time-resolved photoluminescence (TRPL) spectroscopy. As shown in Fig. 4(b), steady-state PL spectra show that the Cu_2O sample exhibits significant luminescence intensity, whereas the PL intensity of the Cu/Cu_2O Schottky junction is quenched, indicating strong suppression of the carrier recombination process. TRPL spectra (Fig. 4(c)) further characterized the carrier lifetime, the shorter fluorescence lifetime of Cu/Cu_2O (τ_1 = 1.1 ns) compared to that of Cu_2O (τ_2 = 11.6 ns) further demonstrates that the Schottky junction enables higher photogenerated carrier separation efficiency. This reduction in lifetime is attributed to the rapid extraction of charge carriers by the strong built-in electric field at the Schottky interface, carriers are rapidly extracted and separated by the Schottky junction before radiative recombination can occur [44, 45]. Electrochemical test results further confirm the higher carrier separation and transport efficiency of Cu/Cu_2O. The linear sweep voltammetry (LSV) curves (Fig. S7(a) in the ESM) confirm that the lower overpotential of Cu/Cu_2O indicates its enhanced electron-hole separation capability. Meanwhile, the Cu/Cu_2O Schottky junction exhibits a decreased impedance semicircle diameter (Fig. S7(b) in the ESM) and a significantly enhanced photocurrent density (Fig. S7(c) in the ESM). These results indicate that the Cu/Cu_2O Schottky junction is conducive to charge carrier separation and transport.

Carrier dynamics were further analyzed on an ultrafast timescale using femtosecond transient absorption spectroscopy (fs-TAS) to investigate the influence of the Schottky junction. Fs-TAS results are shown in Figs. 4(d)–4(i). A 360 nm pump laser was applied to excite both Cu_2O and Cu/Cu_2O. Figures 4(d) and 4(e) show the fs-TAS spectra of the Cu_2O sample. A strong negative ΔA signal was observed near 360 nm, attributed to ground-state bleaching (GSB) generated around this wavelength. Concurrently, a weak positive ΔA signal in the 500–650 nm range was assigned to excited-state absorption (ESA). The ESA signal intensity decayed rapidly with increasing delay time, approaching the baseline. In contrast, the GSB signal amplitude of the Cu/Cu_2O sample (Figs. 4(g) and 4(h)) was smaller (approximately −6 mOD), significantly lower than that of the Cu_2O sample (−15 mOD). The ESA signal reached its maximum intensity at 5 ps and decayed slowly with prolonged pump time. This slowed decay process can be attributed to the strong built-in electric field established upon the formation of the Schottky junction, which drives the transfer of holes to Cu, thereby achieving spatial separation of electrons and holes and suppressing carrier recombination [46].

Unlike TRPL, which probes the radiative recombination pathway, fs-TAS tracks the evolution of the total excited-state carrier population. The fs-TAS decay kinetics of Cu_2O and Cu/Cu_2O were fitted using a tri-exponential function (fitting parameters are provided in the ESM), with the fitting results shown in Figs. 4(f) and 4(i). The fitting yielded an average lifetime ($\tau_{average}$) of 3692.69 ps for Cu_2O. The decay component τ_1 = 5.01 ps can be attributed to the trapping of excited electrons by shallow trap states. The decay component τ_2 (398.31 ps) corresponds to the process of electrons being captured by deep trap states and the decay component τ_3 (3804.36 ps) corresponds to the recombination process of electrons with holes in the valence band (Fig. 4(j)). For Cu/Cu_2O, the built-in electric field generated by the Schottky electrons being captured by deep trap states and the decay component τ_3 (3804.36 ps) corresponds to the recombination process of electrons with holes in the valence band. For Cu/Cu_2O, the built-in electric field generated by the Schottky junction reconstructs the carrier transport process, leading to a significantly extended average lifetime ($\tau_{average}$ = 5014.58 ps). The decay component τ_1 (5.64 ps) corresponds to a shallow trapping process. The decay component τ_2 for Cu/Cu_2O (287.78 ps) is significantly shorter compared to that of Cu_2O, which is attributed to a higher concentration of OVs accelerating electron capture by deep trap states. The decay component τ_3 (5143.99 ps) is substantially longer than that of Cu_2O (3692.69 ps), as the recombination of photogenerated electrons and holes is suppressed by the Schottky junction, enabling effective separation (Fig. 4(k)). The formation of the Schottky junction not only enables rapid carrier extraction but also effectively suppresses recombination through spatial charge separation. This synergistic mechanism ensures efficient carrier utilization, laying a solid kinetic foundation for the superior NIR-driven photothermal catalytic performance of Cu/Cu_2O.

3.3 Photocatalytic performances

To deeply understand the mechanism of NIR light-driven photothermal catalysis in the purification of antibiotics, we selected TC, which is difficult to degrade, as the evaluation object to investigate the degradation performance of Cu/Cu_2O and Cu_2O samples. The TC adsorption experiments were carried out before the photothermal catalytic experiment. It can be observed from Fig. 5(a) that Cu/Cu_2O sample achieves the adsorption–desorption equilibrium after 1 h under dark conditions. The adsorption amount of TC molecules is higher due to the existence of more OVs on the surface of the Cu/Cu_2O sample. The photothermal

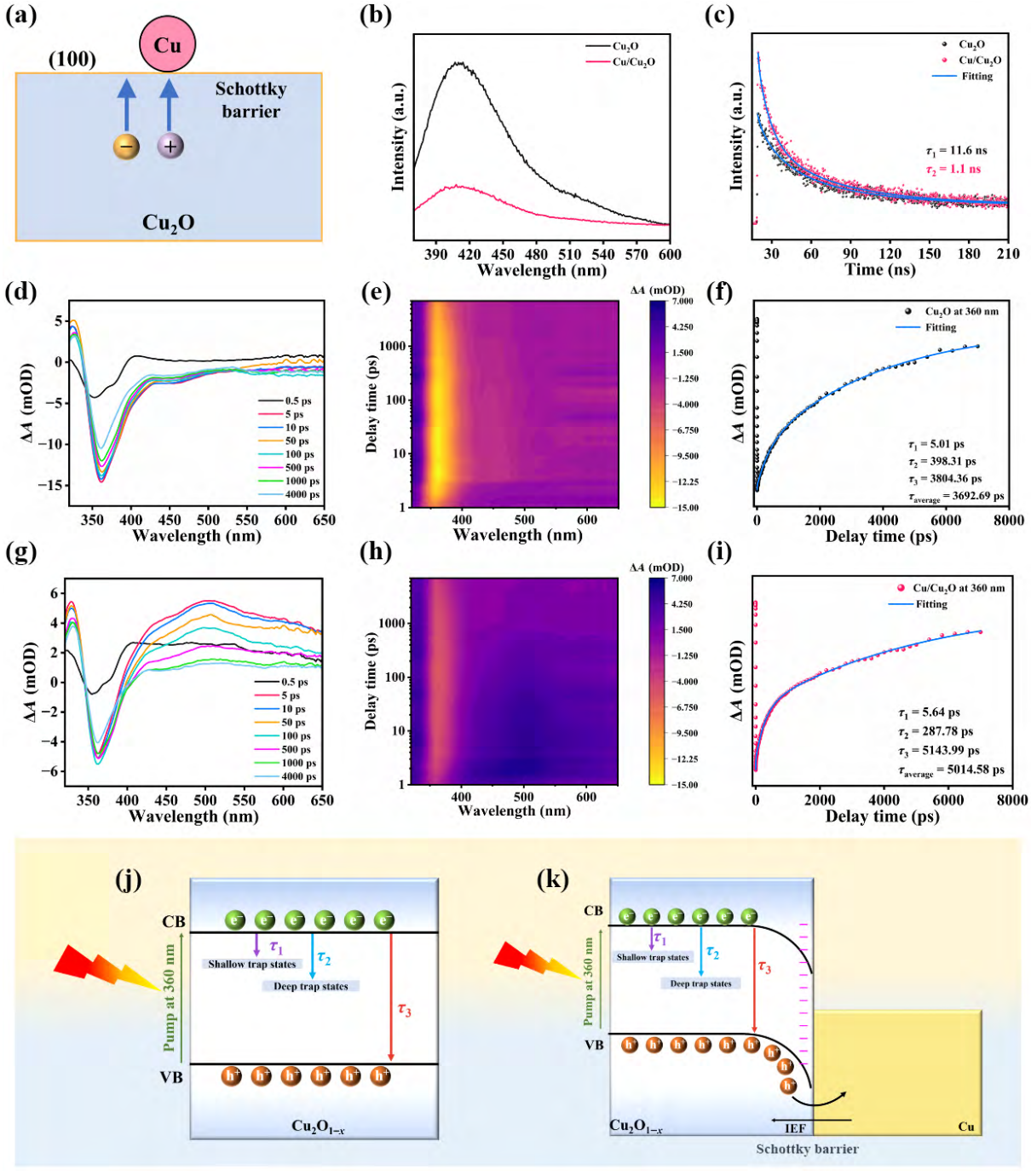

Figure 4 (a) Schematic diagram of charge transfer at the Cu_2O-Cu interface in the Cu/Cu_2O. (b) PL spectra and (c) TRPL decay spectra of Cu_2O and Cu/Cu_2O sample. fs-TAS: (d) fs-TAS of Cu_2O under 360 nm pump at different pump-probe delay time, (e) 2D pseudo-color of fs-TAS and (f) normalized fs-TA decay curves of Cu_2O at 360 nm. (g) fs-TAS of Cu/Cu_2O under 360 nm pump at different pump-probe delay time. (h) 2D pseudo-color of fs-TAS and (i) normalized fs-TA decay curves of Cu/Cu_2O at 360 nm. Photodynamic process of (j) Cu_2O and (k) Cu/Cu_2O concluded from fs-TAS.

degradation experiment was driven by a Xenon lamp (300 W) fitted with an UV–vis light cut off filter (λ > 700 nm). As shown in Fig. 5(b), the Cu/Cu_2O composites achieved a higher tetracycline (TC) degradation rate under 120 min of NIR irradiation compared to the Cu_2O sample. As quantified by the first-order pseudo-kinetics in Fig. 5(c), the Cu/Cu_2O composites exhibited a rate constant of 0.0154 min^{-1}, surpassing the value for Cu_2O (0.0074 min^{-1}) by a factor of 2.1. Additionally, to exclude the influence of the *in-situ* formation of Cu_xO species, degradation experiments of Cu nanoparticles were tested (Fig. S8 in the ESM). Under identical conditions, the degradation efficiency was only 31%, lower than that of the Cu/Cu_2O (85.1%). This indicates that the Schottky interface and OVs are indispensable for achieving high-efficiency photothermal catalysis. Furthermore, the versatility of the Cu/Cu_2O was evaluated under different spectral illuminations. As shown in Fig. S9 in the ESM, the degradation efficiency is higher than that under NIR light alone (λ > 700 nm) under visible and NIR light (λ > 420 nm) and full spectrum illumination. These

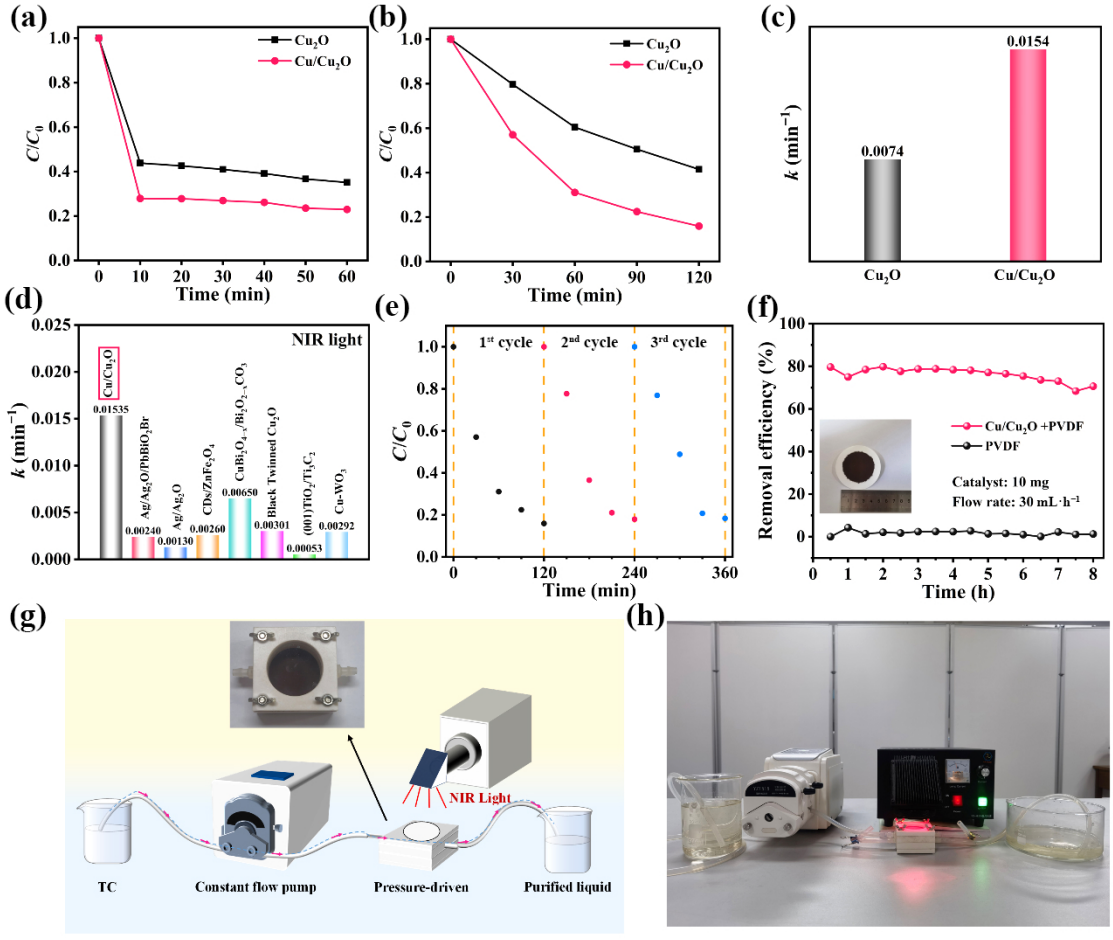

Figure 5 (a) Adsorption curves, (b) photothermal degradation curves, and (c) the corresponding kinetic constants *k* for TC of the Cu_2O and Cu/Cu_2O composites under NIR light irradiation. (d) Evaluation of recent NIR Light-responsive catalysts for TC degradation. (e) Recycle performances of the Cu/Cu_2O composites. (f) Photocatalytic purification performance for TC by using the continuous flow reactor (inset: photograph of catalyst on PVDF membrane). (g) Schematic diagram and (h) photograph of the continuous flow reactor.

results demonstrate that the as-prepared Cu/Cu_2O possesses a broad-spectrum response, enabling more efficient solar energy harvesting and utilization. Compared with previous literature, the prepared Cu/Cu_2O composites exhibit better degradation efficiency and *k* values under NIR light-driven conditions than most similar materials (Fig. 5(d) and Table S1 in the ESM). In addition, the stability of Cu/Cu_2O was studied through three consecutive photodegradation experiments. There is no obvious decrease in the degradation rate in each round, and the degradation efficiency decreases by approximately 2% (Fig. S10(d) in the ESM), indicating an excellent recyclability (Fig. 5(e)). Compared with the sample before degradation, there are no obvious changes in the XRD patterns (Fig. S10(e) in the ESM) and TEM images (Fig. S10(f) in the ESM) of the degraded sample, further indicating that Cu/Cu_2O has a relatively stable microstructure. Figure 5(f) showed that under continuous-flow conditions (30 $mL·h^{-1}$), 10 mg Cu/Cu_2O composites sustained approximately 70% degradation efficiency of TC after 8 h under NIR illumination. The stability and secondary pollution risks of the Cu/Cu_2O catalyst were further evaluated by quantifying the Cu leaching using inductively coupled plasma-mass spectrometry (ICP-MS). The Cu concentration in the treated effluent remained as low as 9.9034 $\mu g·L^{-1}$ (Table S2 in the ESM), well within the safe limit of 1 $mg·L^{-1}$ stipulated by standards for drinking water quality. This further confirms the catalytic stability and practical applicability in water treatment of the Cu/Cu_2O. To evaluate the potential of the Cu/Cu_2O sample in practical applications, the effects of different influencing factors such as pollutant concentration, interferences from different anions and cations, and pH values on the degradation of the TC solution are further investigated under the NIR spectrum through batch experiments. The corresponding results, detailed analysis, and discussions are shown in Fig. S12 in the ESM. Based on the above results, the prepared Cu/Cu_2O composite is a potential candidate material for the removal of antibiotic wastewater.

The temperature changes and the photothermal conversion performances of the catalysts were evaluated via an online thermal camera. As shown in Fig. S13 in the ESM, temperature is indicated by color intensity, with the scale showing a gradient from blue (cooler) to orange (warmer). Control measurements show that NIR irradiation for 1.5 h raises the temperature of the aqueous solution only slightly from 29.9 to 41.3 °C (Fig. S13(a) in the ESM) in the absence of a photocatalyst. The presence of a photocatalyst induces a pronounced photothermal effect, with solution temperature increasing substantially. Particularly, The Cu/Cu_2O demonstrated rapid NIR-driven heating, attaining a final temperature of 49.3 °C (Fig. S13(c) in the ESM) that exceeds the maximum temperature reached by the Cu_2O system (Fig. S13(b) in the ESM). The effect of temperature changes on catalytic activity was elucidated by heating

the TC solution with the Cu_2O sample to 49.3 °C (matching the steady-state temperature of Cu/Cu_2O under NIR light). Under the same thermal conditions, Cu/Cu_2O also exhibited higher degradation efficiency than Cu_2O (Fig. S14 in the ESM). The superior performance of Cu/Cu_2O is attributed to the synergistic effect of hot-electron-driven O_2 activation and the accelerated charge separation at the pre-constructed Schottky interface. To clarify the separate roles of photocatalysis and thermal catalysis in the synergistic photothermal degradation, quantitative comparative experiments were performed. As shown in Figs. S13(e) and S13(f) in the ESM, the degradation rate of TC by the Cu/Cu_2O sample under only NIR light conditions (photocatalysis) at room temperature (k = 0.0031 min^{-1}) is 33.4%. In contrast, when the steady-state photothermal temperature (49.3 °C) was simulated under dark conditions (thermal catalysis), the degradation rate increases to 79.3% (k = 0.0138 min^{-1}). Notably, the kinetic constant for the thermal process is approximately 4.8 times that of pure photocatalysis, underscoring that the NIR-induced thermal effect is the primary driver for accelerating the reaction. To further quantitatively evaluate the photothermal contribution, the kinetics at different reaction temperatures were investigated. As shown in Figs. S13(g) and S13(h) in the ESM, the TC degradation by Cu/Cu_2O at different controlled temperatures (20, 30, 40 and 50 °C) with/without NIR irradiation were evaluated. The results indicate that the k values follow the Arrhenius relationship with temperature (Fig. S13(i) in the ESM). According to the slope of the Arrhenius equation ($\ln k = -E_a/RT + \ln A$), the apparent activation energy (E_a) of photothermal catalysis (5.16 $kJ{\cdot}mol^{-1}$) is significantly lower than that of thermal catalysis (8.43 $kJ{\cdot}mol^{-1}$). The lower E_a value indicates that the superior degradation activity of Cu/Cu_2O is the result of photo-thermal synergy. The photothermal effect accelerates the activation of molecular oxygen kinetically and significantly reduces the reaction energy barrier of O_2 activation, further enhancing the degradation performance of Cu/Cu_2O.

To clarify the possible pathway of TC photodegradation, the intermediate products were detected by a liquid chromatography equipped with mass spectrometry (LC-MS). As shown in Fig. 6(a), nine intermediates were produced with m/z values of 430, 388, 362, 340, 322, 300, 227, 218, 118, 114, 74, and 60, and three possible photodegradation pathways were proposed (see the ESM). First, 4-cyclodimethylamine dealkylation in pathway I TC molecule (m/z = 445) is easily attacked by active groups and degraded to P1 (m/z = 430). With the oxidation reaction of $-NH_2$, CH_3, and –OH groups after being attacked, the fourth benzene ring is cracked to get P2 (m/z = 322), P2 continues to be oxidized by deamination and ring-opening to yield P3 (m/z = 218) [47, 48]. In pathway II, carbon-carbon double bonds in TC molecules can be continuously attacked by ROS and converted into hydroxyl groups. Then, the intermediates undergo the dealkylation and hydroxylation, accompanied by the loss of an acetamide group, resulting in P4 (m/z = 362). And P4 is further converted to P5 (m/z = 340) through continuous dehydrogenation reactions. P5 undergoes further transformation to yield P6 (m/z = 227) through a continuous attacking by reactive oxygen radicals [49]. In pathway III, intermediate P7 (m/z = 388) was formed due to the further loss of the hydroxyl group after the deletion of N-methyl from the TC molecule; followed by the formation of intermediate P8 (m/z = 340) after deamidation and demethylation. And P8 is further converted to P9 (m/z = 300) through dehydroxylation and ring-opening [50]. Subsequently, these intermediates are further attacked by reactive

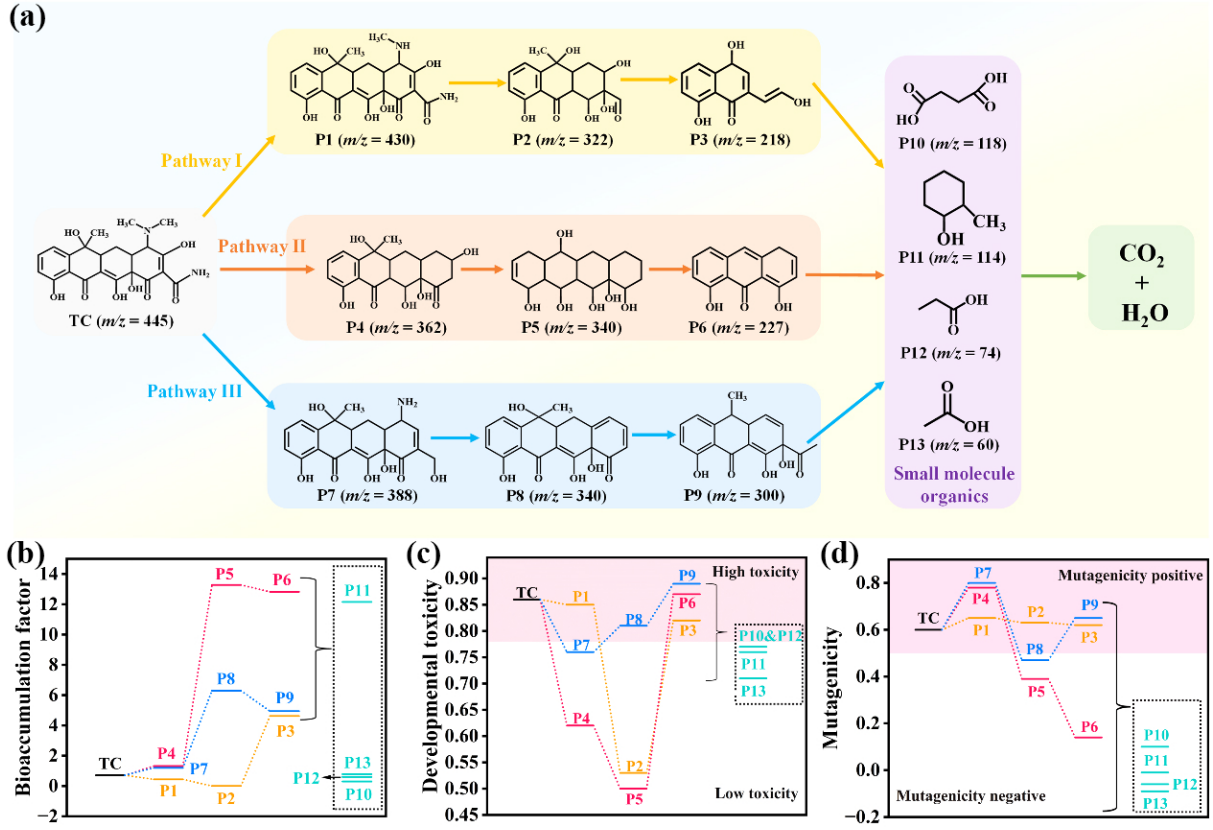

Figure 6 (a) Possible pathways of NIR light-driven TC degradation by using Cu/Cu_2O. (b) Bioaccumulation factor. (c) Developmental toxicity and (d) mutagenicity of TC and their degradation intermediates.

radicals to form other small molecule intermediates such as P10, P11, P12, and P13 (m/z = 118, 114, 74, and 60). To further validate the mineralization capability of the Cu/Cu_2O, TOC removal was measured (Fig. S15 in the ESM). After 120 min of NIR irradiation, the TOC removal efficiency reached 55.01% (from 32.30 to 14.53 mg·L^{-1}). As the photodegradation process continued, the above small molecules will ultimately be decomposed into CO_2 and H_2O.

The bioaccumulation factors, developmental toxicity, and mutagenicity of TC and its corresponding intermediates were evaluated through the toxicity estimation software (T.E.S.T.) based on quantitative structure–activity relationships (QSAR) [51, 52]. It is obvious that the bioaccumulation factor values of small molecular intermediates such as P10, P12, and P13 are low (Fig. 6(b)). The developmental toxicity of most of the photocatalytic degradation intermediates is at the "low toxicity" level (Fig. 6(c)). Although the toxicity of some intermediates shows an increasing trend during the degradation process, with further decomposition, the toxicity of small molecules will be greatly reduced and all will be at the "low toxicity" level, and finally they will be transformed into small molecules such as H_2O and CO_2 with low toxicity within the harmless range. Regarding the corresponding mutagenicity (Fig. 6(d)), TC and the initial intermediates are mutagenic positive (greater than 0.5), and as the degradation proceeds, the mutagenicity of macromolecular intermediates decreases during the degradation process. Small molecular intermediates such as P8, P5, P10, P12, and P13 become mutagenic negative due to their low mutagenic activity (less than 0.5). The above results indicate that the photocatalytic process of Cu/Cu_2O can not only efficiently degrade TC but also reduce its ecological toxicity. Therefore, the constructed photocatalytic system can be regarded as a green technology due to its toxicity attenuation characteristics, and it shows great practical potential in eliminating TC in the water environment.

3.4 Photocatalytic mechanism

ROS play a crucial role in the degradation of TC molecules. To elucidate the degradation mechanism of the synthesized Cu/Cu_2O composite, the formation of ROS during the catalytic reaction was systematically investigated. Scavenger experiments were first conducted using p-benzoquinone (PBQ), 2,2,6,6-tetramethylpiperidine (TEMP), ethylene glycol (EG), and methanol (MeOH) as quenchers for $\cdot O_2^-$, $^1O_2$, h^+, and ·OH, respectively. As illustrated in Figs. 7(a) and 7(b), the degradation efficiency of TC by Cu/Cu_2O decreased from 85.1% to 41.5% upon the addition of MeOH, while the introduction of TEMP, EG, and PBQ reduced the efficiency to 45.9%, 61.9%, and 37%, respectively. These results indicate that the relative contribution of ROS follows the order: $\cdot O_2^- > \cdot OH > {}^1O_2 > h^+$.

EPR spectroscopy further confirmed the generation of these ROS. Using 5,5-dimethyl-1-pyrroline N-oxide (DMPO) as a spin-trapping agent for ·OH and $\cdot O_2^-$, and TEMP and 2,2,6,6-tetramethylpiperidine-1-oxyl (TEMPO) for $^1O_2$ and h^+ respectively, the presence of ROS was verified under NIR irradiation. As shown in Figs. 7(c) and 7(d), the characteristic signals of DMPO-$\cdot O_2^-$ and TEMP-$^1O_2$ were weak in the dark but intensified significantly under NIR light. This enhancement results from the increased generation of e^- driven by photothermal excitation, which facilitates the reduction of dissolved oxygen to form $\cdot O_2^-$. The more pronounced TEMP-$^1O_2$ signal may arise from electron-rich OVs in Cu/Cu_2O promoting the conversion of $\cdot O_2^-$ to $^1O_2$ through reaction with photogenerated h^+, as supported by previous studies [53, 54]. The characteristic DMPO-·OH adduct signal was also observed under irradiation (Fig. 7(e)). Over time, the intensities of DMPO-$\cdot O_2^-$ and DMPO-·OH signals decreased, while that of TEMP-$^1O_2$ increased, suggesting possible conversion of $\cdot O_2^-$ and ·OH to $^1O_2$. Additionally, the decay of the TEMPO signal under NIR light (Fig. 7(f)) indicated the consumption of h^+, confirming their involvement in the photocatalytic process [55]. As shown in Fig. 7(g), under the N_2 atmosphere, the signals of $\cdot O_2^-$, ·OH, and $^1O_2$ all decrease substantially. This indicated that the ROS generated in the system mainly originates from O_2.

To further illustrate the O_2 activation mechanism, *in-situ* diffuse reflectance infrared Fourier transform spectroscopy (*in-situ* DRIFTS) was employed under an O_2 atmosphere with NIR irradiation. As shown in Fig. 7(h), no significant absorption was observed in the absence of O_2 and light. After introducing O_2 in the dark, weak bands appeared at 1130 and 934 cm^{-1}, assigned to the stretching vibrations of $\cdot O_2^-$ and surface-adsorbed O_2, respectively [56–58]. These findings align with the EPR and XPS results, indicating initial O_2 adsorption even without illumination. Under NIR illumination, the absorption intensities intensify significantly and continue to grow with extended exposure time. This enhancement is due to photoinduced and hot electrons generated by the photothermal effect, which concurrently drive the reduction of adsorbed O_2 to yield $\cdot O_2^-$ radicals.

DFT calculations provided insight into the O_2 activation process on different models: pristine Cu_2O, Cu_2O with an oxygen vacancy (Cu_2O_{1-x}), and the Cu/Cu_2O_{1-x} interface (Fig. S17 in the ESM). An evolutionary pathway of oxygen activation capability was clearly revealed, ascending from the inert basal plane of pristine Cu_2O, through the activated landscape of Cu_2O_{1-x}, to the highly synergistic interface of Cu/Cu_2O_{1-x}. At the culmination of this pathway, the composite interface exhibits a remarkable "directional anchoring" effect on the O_2 molecule. One oxygen atom is preferentially captured by the oxygen vacancy, while the other forms a polar bond with the adjacent low-coordination Cu^0 site. This dual-site cooperation triggers a substantial electron transfer of 0.97 e^- from the interface to the O_2 molecule, directly resulting in a pronounced elongation of the O–O bond from 1.208 Å in its free state to 1.474 Å. This critical weakening of the O–O bond effectively lowers the energy barrier for its activation, providing a fundamental electronic-level explanation for the dramatically enhanced catalytic activity observed in experiments.

This evolutionary pathway is quantitatively substantiated by the following calculations on each model. For pristine Cu_2O (Fig. 7(j)), the d-band center of Cu was located at –2.12 eV (Fig. S18(a) in the ESM), far from the Fermi level, resulting in weak orbital hybridization with O_2. The corresponding O_2 adsorption energy was positive of 0.37 eV, with a minimal electron transfer of 0.03 e and a slight O–O bond elongation to 1.235 Å (Fig. 7(i)), indicating poor O_2 activation. Introducing OVs into Cu_2O (Fig. 7(k)) led to unsaturated coordination of surface Cu^+, shifting the d-band center to –1.42 eV (Fig. S18(b) in the ESM) and increasing electron density around Cu sites. This enhanced the O_2 adsorption energy to –1.95 eV, with 0.75 e transferred from Cu_2O_{1-x} to O_2, elongating the O–O bond to 1.461 Å. The positively charged OVs acted as anchoring sites for O_2, promoting electron transfer and facilitating O_2 activation even without light [59]. At the Cu/Cu_2O_{1-x} interface (Fig. 7(l)), the synergistic effect of OVs and metallic Cu created an ideal environment for O_2 activation. The work function difference

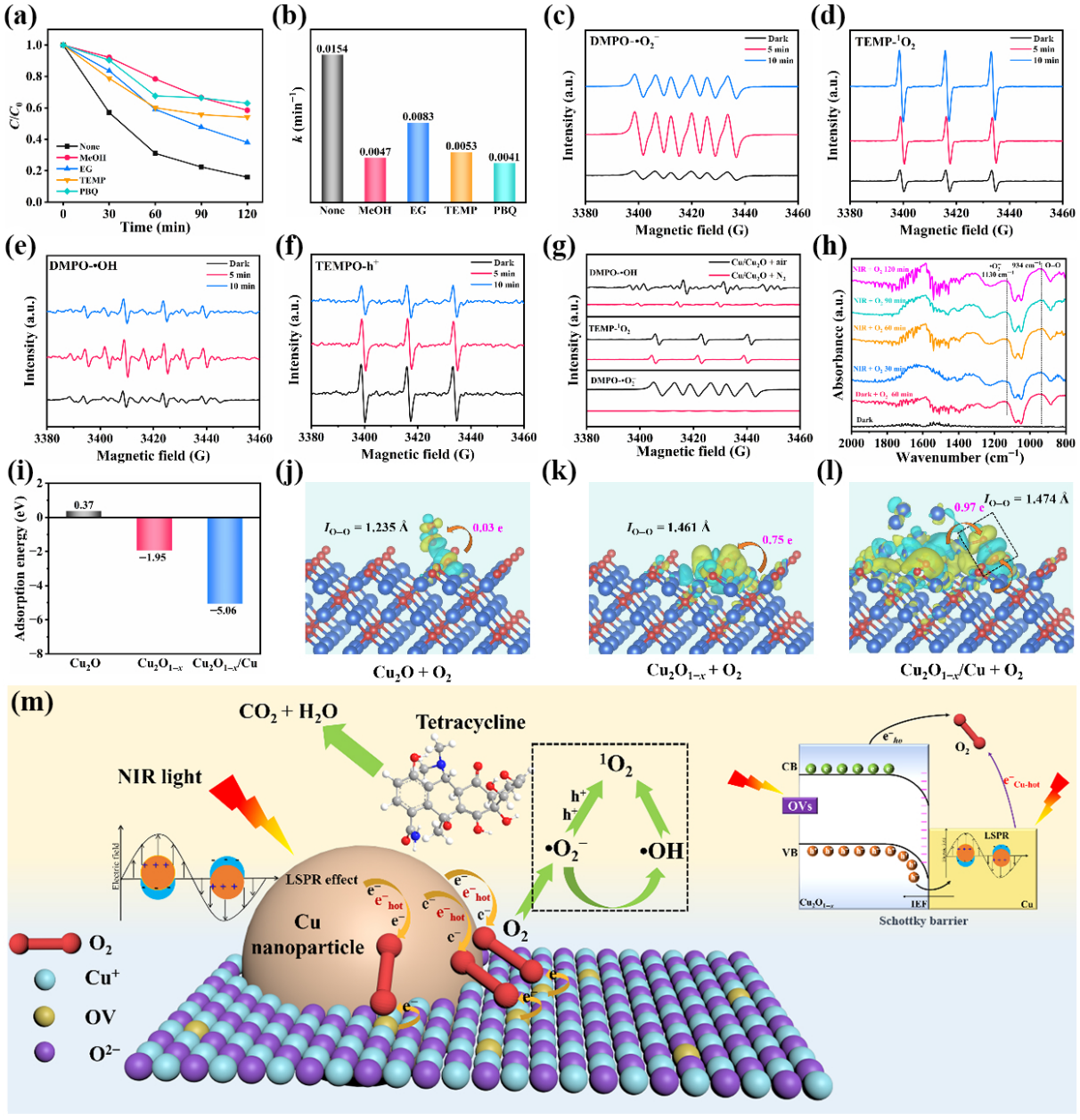

Figure 7 (a) The effect of radical scavengers on the photodegradation performance of Cu/Cu_2O composites under NIR light irradiation and (b) corresponding *k* values. EPR spectra of different radical species: (c) DMPO-·O_2^-, (d) TEMP-$^1O_2$, (e) DMPO-·OH, and (f) TEMPO-h^+. (g) EPR spectra under different atmosphere conditions. (h) *In-situ* DRIFT of Cu/Cu_2O composite under O_2 atmosphere and NIR light irradiation. (i) Adsorption energy of O_2 on the different models. Charge transfer of different models: (j) Cu_2O, (k) Cu_2O_{1-x} (OVs-rich Cu_2O), and (l) Cu_2O_{1-x}/Cu. (m) Schematic diagram of photocatalytic mechanism of Cu/Cu_2O under NIR light.

between Cu (4.34 eV) and Cu_2O (6.92 eV) directed electron transfer from Cu_2O to Cu. This interfacial charge enrichment shifted the d-band center of Cu^0 to −1.57 eV (Fig. S18(c) in the ESM), significantly strengthening O_2 adsorption (E_{ads} = −5.06 eV). The "directional anchoring" mechanism was evident: the incorporation of one O atom into the OV site involved electron acceptance from Cu^+, while the simultaneous binding of the other O atom to Cu^0 also involved charge transfer. This synergistic electron donation (totaling 0.97 e) from both Cu sites into the O_2 molecule populated its antibonding orbitals, leading to the observed substantial elongation of the O–O bond to 1.474 Å and making its activation highly favorable (Fig. S19 in the ESM) [60–62].

Based on these findings, a comprehensive mechanism for NIR-driven photothermal catalysis over Cu/Cu_2O is proposed (Fig. 7(m)). Under NIR irradiation, Cu_2O generates photogenerated electrons ($e^-_{hυ}$) and holes (h^+) (Eq. (1)), while the Schottky junction at the Cu/Cu_2O interface promotes charge separation. Concurrently, a dual LSPR effect excites hot electrons ($e^-_{Cu\text{-}hot}$), which inject into the conduction band of Cu_2O. Molecular oxygen activation proceeds via a "directional anchoring" mechanism at OV-Cu dual sites, where interfacial electron transfer from both photoexcited and hot electrons significantly weakens the O–O bond. This facilitates the formation of ·O_2^- (Eq. (2)), which further transform into ·OH and $^1O_2$ through reactions with holes and other intermediates (Eqs. (3)–(5)). The photothermal effect generated by dual LSPR elevates the local temperature, kinetically accelerating the step of O_2

activation. The synergy between Schottky junction-enabled charge separation, dual LSPR-enhanced light absorption and hot electron generation, and the unique interfacial activation pathway collectively drives the efficient degradation of organic pollutants (Eq. (6))

$$Cu/Cu_2O + h\nu \rightarrow h^+ + e^-_{h\nu} \quad (1)$$

$$O_2 + e^-_{h\nu/\text{Cu-hot}} \rightarrow {}^{\cdot}O_2^- \quad (2)$$

$${}^{\cdot}O_2^- + 2e^-_{\text{Cu-hot}/h\nu} + 2H^+ \rightarrow \cdot OH + OH^- \quad (3)$$

$${}^{\cdot}O_2^- + h^+ \rightarrow {}^1O_2 \quad (4)$$

$${}^{\cdot}O_2^- + \cdot OH \rightarrow {}^1O_2 + OH^- \quad (5)$$

$$TC + {}^{\cdot}O_2^-/h^+/\cdot OH/{}^1O_2 \rightarrow CO_2 + H_2O + \text{small molecules} \quad (6)$$

4 Conclusion

In summary, oxygen vacancy-enriched Cu/Cu_2O were successfully synthesized via a H_2MoO_4-template-assisted liquid-phase reduction method. The resulting material demonstrated significantly enhanced photothermal degradation performance toward TC under NIR light irradiation compared to pristine Cu_2O. Through a combination of microstructural characterization, XPS, EPR, fs-TAS, *in-situ* DRIFTS, and DFT calculations, the underlying mechanism for the improved photocatalytic activity was elucidated. This enhanced performance can be attributed to the synergistic interplay of three key factors: The formation of Schottky junction at the Cu/Cu_2O interface promotes charge separation, the dual LSPR effect originating from intrinsic LSPR of Cu and the defect-state LSPR induced by OVs enhances photothermal conversion, and the unique "directional anchoring" mechanism facilitates O_2 activation through interfacial electron transfer. This study provides valuable insights for the rational design of efficient NIR-driven photothermal catalysts for environmental remediation applications.

Electronic Supplementary Material: Supplementary material (details of material characterization, experimental, and supplementary figures) is available in the online version of this article at https://doi.org/10.26599/NR.2026.94908781.

Data availability

All data needed to support the conclusions in the paper are presented in the manuscript and the Electronic Supplementary Material. Additional data related to this paper may be requested from the corresponding author upon request.

Acknowledgements

This work was supported by the National Natural Science Foundation of China (NSFC, Nos. 52271228 and 22478316), the Natural Science Foundation of Shaanxi Province (No. 2023-JC-ZD-21), Key R&D Program of Shaanxi Province (No. 2025GH-YBXM-001), Central Guidance for Local Scientific and Technological Development (No. 2025ZY-XCZXZS-26), and Research Project of Incubated Teams at Shaanxi Laboratory of Advanced Materials (No. 2025XCLSXSYS-RZ-04).

Declaration of competing interest

All the contributing authors report no conflict of interests in this work.

Author contribution statement

H. T. W.: Data curation, investigation, visualization, methodology, writing – original draft. S. D. S.: Conceptualization, funding acquisition, project administration, supervision, writing – review & editing. W. S. L.: Formal analysis. H. C.: Formal analysis. X. J. Y.: Investigation. Q. Y.: Investigation. M. Y.: Investigation, methodology, writing – review & editing. J. C.: Formal analysis, visualization, writing – review & editing. All the authors have approved the final manuscript.

Use of AI statement

None.

References

[1] Klein, E. Y.; Impalli, I.; Poleon, S.; Denoel, P.; Cipriano, M.; Van Boeckel, T. P.; Pecetta, S.; Bloom, D. E.; Nandi, A. Global trends in antibiotic consumption during 2016–2023 and future projections through 2030. *Proc. Natl. Acad. Sci. USA* **2024**, *121*, e2411919121.

[2] Acosta, A.; Tirkaso, W.; Nicolli, F.; Van Boeckel, T. P.; Cinardi, G.; Song, J. X. The future of antibiotic use in livestock. *Nat. Commun.* **2025**, *16*, 2469.

[3] Larsson, D. G. J.; Flach, C. F. Antibiotic resistance in the environment. *Nat. Rev. Microbiol.* **2022**, *20*, 257–269.

[4] Wang, M. Y.; Zhao, Y. J.; Miao, H.; Wei, Z. High crystallinity of self-assembled iron phthalocyanine enhanced photocatalytic properties for wastewater treatment. *Environ. Chem. Saf.* **2025**, *1*, 9600040.

[5] Xiao, S. T.; Xie, L.; Gao, Y.; Wang, M.; Geng, W.; Wu, X. Z.; Rodriguez, R. D.; Cheng, L.; Qiu, L.; Cheng, C. Artificial phages with biocatalytic spikes for synergistically eradicating antibiotic-resistant biofilms. *Adv. Mater.* **2024**, *36*, 2404411.

[6] Zhu, K.; Li, X.; Chen, Y. W.; Huang, Y. Z.; Yang, Z. Y.; Guan, G. Q.; Yan, K. Recent advances on the spherical metal oxides for sustainable degradation of antibiotics. *Coord. Chem. Rev.* **2024**, *510*, 215813.

[7] Tan, Z. L.; Mao, J.; Hu, Y. Y.; Xue, F.; Yang, Y. Q.; Wang, L.; Zhu, H. X.; He, H. Fabrication of biomimetic giant waterlily cellulosic adsorption-catalytic material for efficient water purification. *Appl. Catal. B: Environ. Energy* **2025**, *366*, 125063.

[8] Tian, Y. J.; Li, J. Z.; Liu, J. Z.; Meng, J.; Li, J. L. Insights into the microbiological mechanism of antibiotic removal in an aerobic-microaerobic process treating manure-free piggery wastewater. *Chem. Eng. J.* **2024**, *484*, 149634.

[9] Liao, G. F.; Yu, Y. Q.; Liu, X.; Wang, P. Revealing the strain-induced spin polarization effect in MBene for efficient photocatalytic disinfection. *Environ. Chem. Saf.* **2025**, *1*, 9600044.

[10] Wei, Y. W.; Fu, H. F.; Zhao, C.; Zhang, L.; Wang, J. F.; Liu, W.; Wang, C. C. Accurate targeted detoxification of fluoroquinolone antibiotics via Fenton-like reaction catalyzed by asymmetric oxygen vacancy on cobalt-doped In_2O_3. *Appl. Catal. B: Environ. Energy* **2025**, *372*, 125290.

[11] Wang, C.; Mirzaei, A.; Wang, Y.; Chaker, M.; Zhang, Q. Z.; Ma, D. L. Construction of ultrathin $BiVO_4$-Au-Cu_2O nanosheets with multiple charge transfer paths for effective visible-light-driven photocatalytic degradation of tetracycline. *Small Methods* **2025**, *9*, 2301804.

[12] Meng, S. H.; Li, J. L.; Wang, S. Y.; Zhan, S. H.; Hu, W. P.; Li, Y. Homo-hetero double junction coupling weakens exciton effects to enhance selective photocatalytic O_2 activation on carbon nitride. *Adv. Mater.* **2025**, *37*, 2420080.

[13] Yang, M.; Li, H. B.; Liu, F. L.; Sun, S. D.; Mei, J.; Jiao, Y. X.; Cui, J.; Xu, Y.; Song, H. L.; Duan, Z. F. et al. Mechanism insight into oxygen vacancy-dependent effect in Fe_1/TiO_2 single-atom catalyst for highly enhanced photo-Fenton mineralization of phenol. *Appl. Catal. B: Environ. Energy* **2024**, *354*, 124071.

[14] Sun, X. N.; Yang, H.; Xie, J. B.; Teng, G. X.; He, J.; Zhao, Z. L.; Zhang, C. A photocatalyst combined of copper doped ZnO and graphdiyne (Cu/ZnO@GDY) for photocatalytic degradation of tetracycline: Mechanism and application. *Water Res.* **2025**, *278*, 123345.

[15] Zhang, C. C.; Zhao, S. W.; Huang, Q. L.; Liu, J. Q.; Zhang, Q. R. Adsorptive-photocatalytic removal of tetracycline from wastewater by Fe_3O_4-and SnO_2-containing biochar nanocomposites. *Biochar* **2025**, *7*, 38.

[16] Han, C.; Kundu, B. K.; Liang, Y. J.; Sun, Y. J. Near-infrared light-driven photocatalysis with an emphasis on two-photon excitation: Concepts, materials, and applications. *Adv. Mater.* **2024**, *36*, 2307759.

[17] Linic, S.; Christopher, P.; Ingram, D. B. Plasmonic-metal nanostructures for efficient conversion of solar to chemical energy. *Nat. Mater.* **2011**, *10*, 911–921.

[18] Xin, Y.; Yu, K. F.; Zhang, L. T.; Yang, Y. R.; Yuan, H. B.; Li, H. L.; Wang, L. B.; Zeng, J. Copper-based plasmonic catalysis: Recent advances and future perspectives. *Adv. Mater.* **2021**, *33*, 2008145.

[19] Tsao, C. W.; Narra, S.; Kao, J. C.; Lin, Y. C.; Chen, C. Y.; Chin, Y. C.; Huang, Z. J.; Huang, W. H.; Huang, C. C.; Luo, C. W. et al. Dual-plasmonic $Au@Cu_7S_4$ yolk@shell nanocrystals for photocatalytic hydrogen production across visible to near infrared spectral region. *Nat. Commun.* **2024**, *15*, 413.

[20] Xu, M. Y.; Yan, C. L.; Chang, B. Q.; Hou, Y. C.; Wang, H. Q.; Song, X. H.; Zhou, W. Q.; Liu, X.; Yan, Y.; Zhang, J. S. et al. Ag plasmon adjusted single crystal Cu_2O nanoreactor array with ordered charge transport and light multiplication effect for high photocatalytic conversion of CO_2. *Nano Energy.* **2025**, *139*, 110930.

[21] Fang, Z. X.; Zhou, M.; Tao, J. Q.; Hou, Y. D.; Ho, W. K.; Yang, C.; Yu, J. C.; Anpo, M.; Zhang, J. S.; Wang, X. C. Supported Au nanoparticles on crystalline carbon nitride for boosted photocatalytic NO oxidation. *Appl. Catal. B: Environ. Energy* **2025**, *369*, 125164.

[22] Zhang, J. Q.; Chen, H. J.; Duan, X. G.; Sun, H. Q.; Wang, S. B. Photothermal catalysis: From fundamentals to practical applications. *Mater. Today* **2023**, *68*, 234–253.

[23] Xiao, Z. R.; Zhang, L. S.; Tan, X. Y.; Sun, K. H.; Li, J. J.; Pan, L.; Zou, J. J.; Li, G. Z.; Wang, D. S. Advances in oxygen defect-mediated photothermal catalytic CO_2 hydrogenation reduction. *Adv. Funct. Mater.* **2025**, *35*, 2500339.

[24] Li, S. J.; Yang, J. L.; Ruan, X. W.; Cui, X. Q.; Ravi, S. K. Plasmonic nanomaterials in photothermal catalysis and artificial photosynthesis: Hot electron dynamics, design challenges, and future prospects. *Adv. Funct. Mater.* **2026**, *36*, 2503186.

[25] Li, J.; Lou, Z. Z.; Li, B. J. Nanostructured materials with localized surface plasmon resonance for photocatalysis. *Chin. Chem. Lett.* **2022**, *33*, 1154–1168.

[26] Yao, C.; Feng, H. C.; Weng, S. R.; Li, J. X.; Huo, Y. F.; Yan, W. W.; Dong, R. L.; Yang, L. B. Cu_2O_{1-x}-superlattices induced oxygen vacancy for localized surface plasmon resonance. *Nano Lett.* **2025**, *25*, 922–930.

[27] Yang, X. D.; Zheng, J. X.; Wang, J. Y.; Feng, J. S.; Qi, J. J. Tuning the population of W $5d_{xy}$ orbital in WO_{3-x} induced direct electron transfer for photocatalytic water decontamination. *Appl. Catal. B: Environ. Energy* **2026**, *386*, 126364.

[28] Guo, H.; Chen, W. X.; Qiao, X. Q.; Li, C.; Sun, B. J.; Hou, D. F.; Wang, M. D.; Wu, X. Q.; Wu, T.; Chi, R. et al. Skillful promotion of charge separation via defect-mediated built-in electric field and LSPR effect for enhanced photocatalytic activity. *Nano Energy* **2025**, *135*, 110672.

[29] Xia, S. X.; Xin, W. W.; Wang, N.; Guo, J. Y.; Zhang, J.; Tian, C. G.; Wen, L. P.; Jiang, L.; Fu, H. G. Localized surface plasmon resonance effect for near full-spectrum photo-enhanced osmotic energy harvesting. *Angew. Chem., Int. Ed.* **2026**, *65*, e22625.

[30] Shi, Y. Q.; Li, Z. H.; Hao, Q. G.; Li, R. Z.; Li, Y.; Guo, L. N.; Ouyang, S. X.; Yuan, H.; Zhang, T. R. Hydrophobic Fe-based catalyst derived from Prussian blue for enhanced photothermal conversion of syngas to light olefins. *Adv. Funct. Mater.* **2024**, *34*, 2308670.

[31] Zhao, J. Q.; Guo, X. D.; Shi, R.; Waterhouse, G. I. N.; Zhang, X. R.; Dai, Q.; Zhang, T. R. NiFe nanoalloys derived from layered double hydroxides for photothermal synergistic reforming of CH_4 with CO_2. *Adv. Funct. Mater.* **2022**, *32*, 2204056.

[32] Le, T.; Salavati-Fard, T.; Wang, B. Plasmonic energetic electrons drive CO_2 reduction on defective Cu_2O. *ACS Catal.* **2023**, *13*, 6328–6337.

[33] Yang, W. P.; Qi, F. Y.; An, W. J.; Yu, H. C.; Liu, S. T.; Ma, P. P.; Chen, R.; Liu, S. X.; Lou, L. L.; Yu, K. Local electronic structure modulation of interfacial oxygen vacancies promotes the oxygen activation capacity of $Pt/Ce_{1-x}M_xO_{2-\delta}$. *ACS Catal.* **2024**, *14*, 5936–5948.

[34] Dai, X. N.; Hu, Z. H.; Wu, Y.; Yang, T. T.; Ye, Z. H.; Han, H. T.; Zhang, Y.; Yang, Y. L. Enhanced photocatalytic activity through interface-defect engineering: Synergy and process mechanism. *Appl. Catal. B: Environ. Energy* **2025**, *379*, 125667.

[35] Li, X. Y.; Wu, B. H.; Zhang, X. R.; Chen, A. K.; Wang, J. L.; Wang, H. L.; Ciesielski, A.; Liu, J.; Zhang, J. T. Plasmon mediated photocatalysis: Engineering interfaces for effective hot carrier utilization. *ACS Energy Lett.* **2025**, *10*, 1347–1356.

[36] Zhang, X. C.; Sun, S. D.; Wang, H. T.; Lyu, J.; Yu, X. J.; Yang, B.; Yang, M.; Duan, Z. F.; Yang, Q.; Cui, J. Mechanism insight into twin-dependent photocatalysis in near-infrared light-responsive Cu_2O nanocrystals with rich oxygen vacancies. *Nano Mater. Sci.* **2026**, *8*, 49–58.

[37] Li, J. H.; Sun, S. D.; Lyu, J. L.; Yu, X. J.; Zhao, J. Q.; Yang, M.; Yang, B.; Yang, Q.; Cui, J. Mechanistic insight into near-infrared light-driven Cu_2O/WO_2 ohmic contact photothermal catalysts for high-efficiency antibiotic wastewater purification. *Nanoscale* **2024**, *16*, 14116–14129.

[38] Devaraj, M.; Saravanan, R.; Deivasigamani, R.; Gupta, V. K.; Gracia, F.; Jayadevan, S. Fabrication of novel shape Cu and Cu/Cu_2O nanoparticles modified electrode for the determination of dopamine and paracetamol. *J. Mol. Liq.* **2016**, *221*, 930–941.

[39] Yang, Y. M.; Gao, X. N.; Yang, S. J.; Shen, Y. H.; Xie, A. J. Synthesis and superior SERS performance of porous octahedron Cu_2O with oxygen vacancy derived from MOFs. *J. Mater. Sci.* **2021**, *56*, 9702–9711.

[40] Wang, K. F.; Lv, M. R.; Si, T.; Tang, X. N.; Wang, H.; Chen, Y. Y.; Zhou, T. Mechanism analysis of surface structure-regulated Cu_2O in photocatalytic antibacterial process. *J. Hazard. Mater.* **2024**, *461*, 132479.

[41] Gong, Z. H.; Zhong, W. Y.; He, Z. Y.; Liu, Q. Y.; Chen, H. J.; Zhou, D.; Zhang, N.; Kang, X. W.; Chen, Y. Regulating surface oxygen species on copper(I) oxides via plasma treatment for effective reduction of nitrate to ammonia. *Appl. Catal. B: Environ.* **2022**, *305*, 121021.

[42] Liu, X. F.; Kong, L. N.; Xu, J. P.; Lin, Z. Y.; Xu, D. H.; Sun, J. W.; Shi, S. B.; Zhang, X. S.; Li, L. Photothermal catalysis synergy enhances the H_2 evolution performance of $NiS/ZnIn_2S_4$ nanosheet film from macro to micro. *Appl. Catal. B: Environ. Energy* **2026**, *385*, 126298.

[43] Shi, W. L.; Chen, Z. Z.; Lu, J. L.; Sun, X. H.; Wang, Z. Y.; Yan, Y. J.; Guo, F.; Chen, L. Z.; Wang, G. Z. Construction of $ZrC@ZnIn_2S_4$ core–shell heterostructures for boosted near-infrared-light driven photothermal-assisted photocatalytic H_2 evolution. *Chem. Eng. J.* **2023**, *474*, 145690.

[44] Kang, X.; Shi, J. W.; Liu, Y. B.; Mao, L. H.; Zhai, B. J.; Jiang, Y. Z.;

Xiao, W. B.; Jin, H.; Guo, L. J. Supercritical CO_2-induced exfoliation of supramolecular precursor for fabrication of three-dimensional tremella-like g-C_3N_4 with highly efficient photocatalytic H_2 production. *J. Mater. Sci. & Technol.* **2026**, *269*, 24–32.

[45] Yang, W. J.; Si, L. F.; Cheng, C.; Cui, Y. Y.; Yan, X. L.; Liu, M. C.; Jing, D. W.; Shi, J. W.; Guo, L. J. Synergistic integration of atmospheric water harvesting and solar-driven hydrogen production via multifunctional hygroscopic-photocatalytic hydrogel nanocomposite. *Adv. Funct. Mater.* **2026**, *36*, e12738.

[46] Li, Y.; Yu, S.; Xiang, J. L.; Zhang, F. Y.; Jiang, A. Q.; Duan, Y. G.; Tang, C.; Cao, Y. H.; Guo, H.; Zhou, Y. Revealing the importance of hole transfer: Boosting photocatalytic hydrogen evolution by delicate modulation of photogenerated holes. *ACS Catal.* **2023**, *13*, 8281–8292.

[47] Li, W. Q.; Zhou, D.; Jiang, H. W.; Chen, H. Y.; Guo, J. Y.; Yang, J. J.; Wang, X. Y.; Wang, H.; Yuan, X. Z.; Jiang, L. B. MoO_2 co-catalytic Fe^{3+}/periodate for tetracycline degradation: Key role of Fe/Mo cycling and high-Valent iron (Fe(IV)) generation. *Sep. Purif. Technol.* **2024**, *346*, 127509.

[48] Yu, T. T.; Yang, B.; Zhang, R.; Yang, C. Y.; Arramel; Jiang, J. Z. Fabrication of a novel Z-S-scheme photocatalytic fuel cell with the Z-scheme TiO_2/GO/g-C_3N_4 photoanode and S-scheme $BiOAc_{1-x}Br_x$/BiOBr photocathode for TC degradation. *J. Mater. Sci. Technol.* **2024**, *188*, 11–26.

[49] Cui, J.; Zhu, R. T.; Ding, M. Q.; Chen, G. L.; Liang, S. H.; Sun, S. D. Engineering of Bi_2O_3–BiOI 2D/2D S-scheme heterojunction for efficient photocatalytic organic hazards removal. *Sep. Purif. Technol.* **2025**, *354*, 129136.

[50] Sun, K. Q.; Wang, X. W.; Yuan, H.; Hou, J. H.; Shi, W. L.; Li, C. S.; Guo, F. Magnetically separable and recyclable $ZnFe_2O_4$ nanoparticles as an effective activator in resorcinol-formaldehyde resins-based photocatalysis-self-Fenton system. *Sep. Purif. Technol.* **2024**, *351*, 128044.

[51] Li, Q.; Zhou, Q.; Deng, H.; Li, Z. H.; Xue, B.; Liu, A. X.; Shen, B.; Hao, D.; Zhu, H. Y.; Wang, Q. Schottky heterojunction-based photocatalysis-*in-situ*-self-Fenton system: Removal of tetracycline hydrochloride and biotoxicity evaluation of intermediates. *Appl. Catal. B: Environ. Energy* **2025**, *360*, 124533.

[52] Du, H.; Huo, R. B.; Liu, A. X.; Hui, Y. X.; Shen, B.; Li, N. Y.; Ji, Y.; Jin, Q.; Zheng, B. B.; Yang, G. X. et al. Resorcinol-formaldehyde resins/MIL-88A(Fe) S-scheme heterojunctions drive photo-self-Fenton system for enhanced tetracycline degradation and bacterial inactivation: Mechanism insight and DFT calculation. *Appl. Catal. B: Environ. Energy* **2024**, *357*, 124283.

[53] Nosaka, Y.; Nosaka, A. Y. Generation and detection of reactive oxygen species in photocatalysis. *Chem. Rev.* **2017**, *117*, 11302–11336.

[54] Zhang, W. T.; Huang, W. G.; Jin, J. Y.; Gan, Y. H.; Zhang, S. J. Oxygen-vacancy-mediated energy transfer for singlet oxygen generation by diketone-anchored MIL-125. *Appl. Catal. B: Environ.* **2021**, *292*, 120197.

[55] Li, X.; Yang, S. X.; Zhang, F. L.; Zheng, L. Y.; Lang, X. J. Facile synthesis of 2D covalent organic frameworks for cooperative photocatalysis with TEMPO: The selective aerobic oxidation of benzyl amines. *Appl. Catal. B: Environ.* **2022**, *303*, 120846.

[56] Ruan, X. W.; Xu, M. H.; Zhang, X. L.; Ding, C. S.; Meng, D. P.; Leng, J.; Zhang, W.; Ravi, S. K.; Cui, X. Q. Dual plasmonic fields enable high-density hot-electron generation with stepwise charge transfer directed to oxygen reduction sites for enhanced artificial photosynthesis of H_2O_2. *Adv. Energy Mater.* **2025**, *15*, 2502302.

[57] Wang, D. F.; Zhao, W. Z.; Tan, F. Y.; Wang, X.; Dong, J. W.; Zhou, S. Y.; Liu, G. F.; Gu, P. Y. Selective oxygen activation by integrating dual photosensitizers in conjugated porous polymers and microenvironments manipulation for high-performance water purification and H_2O_2 production. *Adv. Funct. Mater.* **2025**, *35*, 2419010.

[58] Yu, W. Y.; Chen, F.; Zhang, X. L.; Tian, N.; Zhang, N.; Zhang, Y. H.; Huang, H. W. Dipole field and locally polarized electric field in asymmetric crystalline carbon nitride for high-efficiency artificial photosynthesis of hydrogen peroxide. *Nano Energy* **2025**, *138*, 110862.

[59] Yu, B.; Liu, P.; He, J. J.; Li, X. J.; Sun, X.; Peng, B. X.; Zhang, J. H.; Ning, Y. Spatially engineering the internal microstructure of a single crystal via nanoparticle occlusion. *Angew. Chem., Int. Ed.* **2025**, *64*, e202505637.

[60] Xie, Z. Q.; Saad, A.; Shang, Y. N.; Wang, Y.; Luo, S.; Wei, Z. S. Enhanced degradation of micropollutants by visible light photocatalysts with strong oxygen activation ability. *Water Res.* **2023**, *247*, 120785.

[61] Sun, Y. D.; Han, W. G.; Zhang, F. Y.; Li, H.; Zhang, Z. Q.; Zhang, X.; Shen, B. X.; Guo, S. Q.; Ma, T. Y. Dual defect regulation of BiOCl halogen layer enables photocatalytic O_2 activation into singlet oxygen for refractory aromatic pollutant removal. *Appl. Catal. B: Environ. Energy* **2024**, *345*, 123689.

[62] Di, G. L.; Shu, R. Y.; Han, D. J.; Ding, J. W.; Chen, Z. F.; Li, X. D.; Wu, X. W.; Zhao, X. L. Oxygen vacancy and boron dual sites enable efficient oxygen activation for emerging contaminant degradation: Boosted exciton dissociation via built-in electric field modulation. *Appl. Catal. B: Environ. Energy* **2025**, *362*, 124754.